2018

Chalcogen Impact on Covalency within Molecular $[Cu_3(\mu_3\text{-}E)]^{3+}$ Clusters (E = O, S, Se): A Synthetic, Spectroscopic, and Computational Study

B. J. Cook

G. N. Di Francesco

R. B. Ferreira

J. T. Lukens

K. E. Silberstein

See next page for additional authors

Authors

B. J. Cook, G. N. Di Francesco, R. B. Ferreira, J. T. Lukens, K. E. Silberstein, B. C. Keegan, V. J. Catalano, K. M. Lancaster, Jason M. Shearer, and L. J. Murray

HHS Public Access

Author manuscript

Inorg Chem. Author manuscript; available in PMC 2019 September 17.

Published in final edited form as:

Inorg Chem. 2018 September 17; 57(18): 11382–11392. doi:10.1021/acs.inorgchem.8b01000.

Chalcogen Impact on Covalency within Molecular $[Cu_3(\mu_3\text{-}E)]^{3+}$ Clusters (E = O, S, Se): A Synthetic, Spectroscopic, and Computational Study

Brian J. Cook[#†], **Gianna N. Di Francesco**[#†], **Ricardo B. Ferreira**[#†], **James T. Lukens**[‡], **Katharine E. Silberstein**[‡], **Brenna C. Keegan**[§], **Vincent J. Catalano**[§], **Kyle M. Lancaster**[‡], **Jason Shearer**[§], and **Leslie J. Murray**[†]

[†] Center for Catalysis and Florida Center for Heterocyclic Compounds, Department of Chemistry, University of Florida, Gainesville FL 32611-7200, U.S.A.

[‡] Department of Chemistry and Chemical Biology, Cornell University, Ithaca, NY 14853, U.S.A.

[§] Department of Chemistry, University of Nevada, Reno, Reno, NV 89557, U.S.A

[#] These authors contributed equally to this work.

Abstract

Reaction of the tricopper(I)-dinitrogen tris(β-diketiminate) cyclophane, $Cu_3(N_2)$**L**, with O-atom transfer reagents or elemental Se afford the oxido-bridged tricopper complex, Cu_3O**L** (**2**), or the corresponding Cu_3Se**L** (**4**), respectively. For **2** and **4**, incorporation of the bridging chalcogen donor was supported by ESI/MS and O or Se K-edge X-ray absorption data. Cu $L_{2,3}$-edge data quantify 53.0% Cu 3*d* character in the LUMO of **2**, with Cu 3*d* participation decreasing to 36.0% in **4** and 43.5% in the related sulfide cluster Cu_3S**L** (**3**). Multiedge XAS and UV/visible/nIR spectra are employed to benchmark DFT calculations, which describe the copper-chalcogen interactions as highly covalent across the series of $[Cu_3(\mu\text{-}E)]^{3+}$ clusters. This result highlights that metal-ligand covalency is not reserved for more formally oxidized metal centers (*i.e.*, $Cu^{III} + O^{2-}$ vs. $Cu^{II} + O^{-}$), but rather is a significant contributor even at more typical ligand field cases (*i.e.*, $Cu_3^{II/II/I} + E^{2-}$). This bonding is reminiscent of that observed in *p*-block elements rather than in early transition metal complexes.

TOC Synopsis:

A family of tricopper cyclophanates bridged by single chalcogenides is synthesized and fully characterized through a suite of physical techniques, including XAS, EXAFS, XANES, as well as computational methods (ROCIS and SORCI). A continual increase in Cu-E covalency is observed from E = O→S→Se, as judged by Cu-$L_{2/3}$ XAS, as well as ligand K-edge XAS. This is coupled

Corresponding Author murray@chem.ufl.edu (LJM) kml236@cornell.edu (KML) shearer@unr.edu (JS).

Notes

The authors declare no competing financial interests.

Supporting Information

Supporting Information available: Spectral (^{1}H NMR, UV-Vis, NIR) data for **2–4**, Electrochemical data for **2–4**, CIF of **4**, SORCI for **2**, raw and fit Cu $L_{2,3}$-edge XAS of **2–4**, sample O-atom transfer reactivity of **2**. Supporting Information is available free of charge via the Internet at http://pubs.acs.org.

to an increase in chalcogen p_z character in the LUMO of Cu_3EL, culminating in 38.6% Se character.

Graphical Abstract

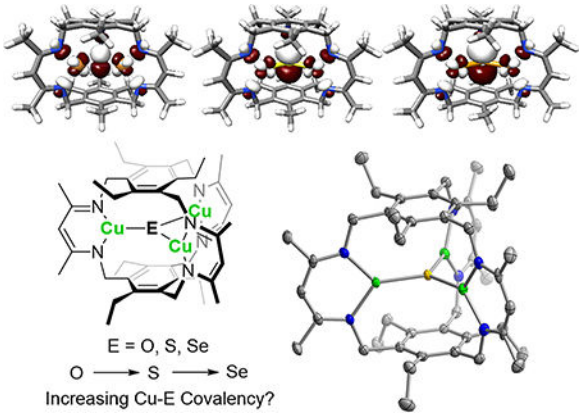

Keywords

Copper chalcogenides; metal-ligand bonding; light atom X-ray Absorption Spectroscopy; inverted ligand field

Introduction

Copper chalcogenides, $Cu_{2-x}E$, have diverse applications, ranging from light harvesting in photovoltaics to sensors and battery materials.[1] The broad utility of the binary, and by extension, the related ternary and quaternary materials, arises from the ease of access to substoichiometric compositions (i.e., intermediate between CuE and Cu_2E), which allows for tunable concentrations of charge carriers, provides for site vacancies for accommodating other ions, and can afford electroluminescence and surface plasmon resonance properties.[2] Despite their growing importance, a detailed understanding of the electronic structure of these materials and consequently the band structure of the extended solids remains lacking. This deficiency is evident; X-ray photoelectron and absorption spectroscopic data are inconsistent with calculated band structures.[3] Model systems that report on the nature of Cu–E interactions, such as the degree of covalency and charge delocalization, are of critical importance to modeling and predicting the properties of this class of materials, including Cu-O zeolites.[4] Molecular copper chalcogenide clusters remain an active area of research with the aim of interrogating the metal-ligand interactions and developing nanoscale models for the bulk materials.

A notable example of the ambiguities surrounding copper-chalcogen bonding concerns studies on an amine-supported $[Cu_3S_2]^{3+}$ cluster reported by Brown, *et al.*[5] Initially, the oxidation states were assigned as two μ_3-sulfides with formally two copper(II) and one copper(III) ion. In light of ongoing electronic structure discussions in which descriptors such as oxo-copper(III) and oxylcopper(II) are frequently advanced, an alternate formalism would invoke ligand based oxidation.[4, 6] Indeed, more recent work – in particular, by Berry and

coworkers[7] – provide strong evidence in support of an alternate electronic structure:[8] a bridging subsulfide or S_2^{3-} couples antiferromagnetically to three copper(II) cations. As alluded to above, copper-oxygen species containing formally high oxidation states (e.g., Cu^{III}), are invoked as reactive intermediates in biological chemistry and catalysis.[6a, 6e, 9] For example, the formally $[Cu^{III}–OH]^{2+}$ moiety has been demonstrated as a potent agent for $H^{\bullet}$ abstraction.[10] However, a number of core-level spectroscopic studies has called into question the physical accuracy of d^8 Cu^{III} assignments.[11] The origin of this ambiguity is suggested to stem from Cu occupying a position where covalent bonding supplants dative, coordinate metal–ligand interactions; coinage metals sit within a boundary region between the main group and the transition elements.[12]

Low-valent multicopper motifs, including $[Cu^{II}_2O]^{2+}$ units, have been identified as the active species in zeolite-based catalysts for methane hydroxylation.[6b, 6c] Arguments have been advanced that such units owe their reactivity to significant oxyl (suboctet $O^{\bullet-}$) character.[6b–d] Similar electronic structure descriptions have been proposed for trigonal planar copper(II) and iron(III) iminyl radical vs. the metal imido formalism.[13] Such arguments can themselves naturally follow from the view of Cu–O motifs as highly covalent units; however, detailed studies aimed at validating such notions for these species are rare. The accepted notion of metal-oxygen covalency is reserved for the highest plausible oxidation states where hole-character is invoked for the ligand, and has not been suggested for typical oxidation states; that is, $Cu^{III}–O^{2-}$ is ambiguous whereas $Cu^{II}–O^{2-}$ is not.

One of our groups has reported the synthesis of a sulfide-bridged complex, $[Cu_3S]$**L** (**3**), from the reaction of S-atom sources (e.g., S_8 or trime-thylphosphine sulfide) with a $Cu^{I}_3–N_2$ complex, **1** (Scheme 1).[14] To advance discussion of electronic structure-function relationships in Cu–E units, we sought to access the corresponding oxide- and selenidebridged congeners and use spectroscopic and computational methods to probe the electronic structure of this series of compounds. To our knowledge, there are no prior examples of an isostructural series of $[Cu_3(\mu_3\text{-}E)]^{3+}$ clusters. For E = S, parallels can be made to the (μ-sulfido)multicopper compounds from Mankad and Hillhouse as well as the aforementioned $[Cu_3S_2]^{3+}$ cluster.[15] For E = O, $[Cu_3O]^{n+}$ clusters supported by pyrazolates (n = 4, 5) or a macrotetracyclic amine (n = 4) have been synthesized and characterized,[16] although reduction to the 3+ state was not reported. Similarly, the 3+ cluster is unknown in enzymatic systems; the closest comparison is the rapid reduction of the native intermediate in multicopper oxidases, a (μ-hydroxo)(μ_3-oxo)tricopper(II) cluster, to the all-cuprous state.[17] All cupric oxide-bridge clusters are well precedent, including a (μ-oxo)tricopper(II) compound reported by Suh and coworkers[16c]; although, the bonding picture in these clusters lacks the ambiguity of the partially oxidized species.

Herein we report the synthesis and characterization of $Cu_3(\mu_3\text{-}O)$**L** (**2**) and $Cu_3(\mu_3\text{-}Se)$**L** (**4**), as well as further spectroscopic studies on the previously reported sulfide-bridged compound, $Cu_3(\mu_3\text{-}S)$**L** (**3**). Using spectroscopic methods including Cu K-, Cu $L_{2,3}$-, and E K-edge X-ray absorption spectroscopy (XAS) coupled to electronic structure calculations, we directly compare the effect of the chalcogen on the electronic structure. In particular, we show that the amount of Cu $3d_\pi$ character in the LUMO diminishes slightly across the series, but nevertheless the Cu–E interactions remain covalent and comparable for the O, S,

and Se compounds. A consistent electronic structure emerges showcasing the highly covalent nature of bonding between copper and all of the chalcogens even in the absence of a formal copper(III) center. Owing to the covalent and delocalized nature of the lowest unoccupied molecular orbital (LUMO) common to all three species, we ultimately deem the assignment of formal oxidation states to the Cu ions in these tricationic clusters (e.g. $Cu^{I}_{2}Cu^{II}$ or $Cu^{I}Cu^{II}_{2}$) to be overly simplistic.

Results and Discussion

Synthesis of 2 and 4.

Using a slightly modified protocol relative to that reported for Cu_3S**L** (**3**), reaction of the dinitrogen-tricopper(I) complex, **1**, with metallic Se at 100 ˚C for 2 h in toluene affords a dark green solution of Cu_3SeL (**4**), which can be isolated from the reaction mixture in an 86% yield (Scheme 1). Substituting the elemental chalcogen for an O-atom donor in the protocol described above, such as trimethylamine *N*-oxide or iodosobenzene, affords the dark brown-yellow microcrystalline product, Cu_3O**L** (**2**), in quantitative yield (Scheme 1). Analogous to the sulfide congener, **2** and **4** are diamagnetic and three-fold symmetric (D_{3h}) on the NMR (^{1}H- and ^{13}C) timescale (Figure S3-S9). For the oxide-bridged compound, we do not observe paramagnetic broadening or shifting in spectra recorded between –85 and 95 ˚C. High-resolution ESI mass spectra on solutions of **2** and **4** agree with formulations of Cu_3O**L** and Cu_3Se**L**, where $\mathbf{L}^{3-}$ is the cyclophanate, $C_{45}H_{63}N_6^{3-}$. In addition, infrared absorption spectra for 2, 3 and 4 are comparable with no evidence for an E–H vibration, which is consistent with the absenceof corresponding E–H resonance in the NMR spectra recorded in anhydrous and air-free solvents.Taken together, our results are consistent with a (μ_3-oxido)- and (μ_3-selenido)-tricopper complexes as the product of net chalcogen substitution of N_2 in **1**. As noted above, complex **2** represents a unique example of a $[Cu_3O]^{3+}$ cluster as all reported oxido-tricopper complexes contain more oxidized clusters; [16a, 16b] spectroscopic and theoretical interrogation of its molecular and electronic structure are discussed below.

X-ray diffraction data obtained from single crystals grown from slow evaporation of a saturated benzene solution of **4** reveal a molecular formula of Cu_3Se**L** (Figure 1). The molecule is isostructural to the S analogue, and consistent with the D_{3h} ^{1}H NMR spectrum as well as the molecular formula obtained from ESI-HRMS. The molecule has near-crystallographic three-fold symmetry in the solid state, with Cu–Se bond lengths statistically identical (2.1942(4), 2.1944(4), 2.1926(4)), and equally similar Cu–N bond lengths (1.908(2)–1.915(3)). Each Cu is trigonal planar, as in **3**. The N–Cu–N bond angles of 101.9–102.3˚ are slightly more acute than the corresponding angle in **3**, owing to the larger size of Se vs. S. The Cu–Se bond lengths are much shorter than those reported for typical Cu–Se single bonds (2.302–2.524 Å),[18] and could arise from Cu–Se multiple bonding character or as a consequence of the geometric constraints imposed by the ligand.

Despite multiple attempts to obtain X-ray quality crystals of **2**, we were able to obtain only microcrystalline powders. Therefore, we utilized Cu K-edge X-ray absorption spectroscopy (XAS) to obtain structural information for **2**. The EXAFS region of the Cu K-edge XAS of **2**

is best fit with two Cu–N scatterers at 1.98 Å and a shorter Cu–O scatterer at 1.87 Å (Figure 2). The separation of the N/O scatterers is warranted by the quality of the data; it is expected that two shells separated by 0.12 Å or more is resolvable for the *k*-space range the data for **2** was analyzed over. Comparable Cu–N bond distances are observed for **1** (*viz.* 1.8805, 1.9278 Å) and for the (μ_3-sulfido)tricopper cyclophanate (*viz.* 1.930– 1.936 Å) (Table 1).[14, 20] Cu–C single scatter pathways found between 2.0–3.5 Å in the k^3 FT EXAFS spectrum resulting from scattering by the ligand scaffold could be successfully modelled. This model is thus consistent with the proposed $[Cu_3(\mu_3\text{-}O)]^{3+}$ core supported by the cyclophane ligand.

Cu K-edge XANES of 2–4.

To define the electronic structure of **2** and understand how it is influenced by changing the central chalcogen ligand, we performed X-ray absorption spectroscopic studies combined with electronic structure calculations. The Cu K-edge XANES of **2** (Figure 3) features a weak pre-edge peak at 8978.7(2) eV, corresponding to a formally dipole-forbidden, quadrupole-allowed Cu 1 $s \rightarrow 3d$ excitation.

A pronounced shoulder is present at 8985.7(2) eV, which by convention we assign as formally dipole-allowed Cu $1s \rightarrow 4p$ + LMCT shakedown transitions (vide infra).[19] The rising edge inflection point in the XANES of **2** is at 8986.6(1) eV, which is blue shifted by 4.1 eV relative to the $Cu_3(N_2)$**L** precursor, **1** (8982.5(1) eV). We have previously communicated that **1** is best described as a closed shell d^{10} Cu^{I}_3 complex,[20] and the increase in edge energy exhibited by **2** suggests increased positive charge at the Cu nuclei relative to **1**. This result supports oxidation of the Cu_3 core upon incorporation of the O-atom bridge in **2**.

The Cu K-edge XANES observed for complexes 3 and 4 (Figure 3) are different from 2, but strikingly similar to one another. Each lack a resolved Cu 1 $s \rightarrow 3d$ transition and display intense shoulders at 8984.4(2) eV corresponding to Cu $1s \rightarrow 4p$ + LMCT shakedown transitions. Furthermore, the rising-edge inflection point for 3 and 4 is slightly redshifted by 0.5 eV to 8986.1(1) eV. The combination of a red-shift in the edge coupled with a substantial decrease in the intensity of the Cu 1 $s \rightarrow 3d$ transition (vide infra) both indicate a reduction in Cu hole character to the low energy acceptor states. This conclusion is supported by Cu Ledge XAS and electronic structure calculations (vide infra).

Cu $L_{2/3}$-edge XAS on 2–4.

The Cu $L_{2/3}$-edge XAS of **2** is displayed in Figure 4. Major peaks are conventionally assigned as Cu $2p \rightarrow 3d$ excitations. $L_{2,3}$ peak energies for **2**–**4** are compiled in Table 2. L_3 peaks ca. 930.8–931.5 eV, which systematically increase in energy upon going from **2** to **4**, are typical for Cu(II) species (and ca. 2 eV lower than those of bona fide Cu(III) species).[21] It should be noted, however, that both inverted bonding schemes and XAS-MLCT features can complicate comparisons of XAS energies.[11a, 22] Using the $L_{2,3}$-edge XAS of D_{4h} $(nmph)_2[CuCl_4]$ (with 61% Cu 3d character in its singly occupied molecular orbital (SOMO)) as a standard,[23] the total integrated area of the L_3 and L_2 peaks in the spectrum of **2** report 16.5(4)% Cu $3d$ character per hole in the acceptor MO. Given three Cu centers, these values amount to a total Cu $3d$ contribution of 50(1)% per hole. Thus, the $L_{2,3}$edge

XAS report the absence of 1.06 electrons between the three Cu centers. Progressively more Cu^{I} character is attained as the chalcogen is varied from O to Se; S-containing **3** possesses 41(1)% Cu character per hole while Se-containing **4** possesses 31(1)% Cu character per hole.

Ligand K-edge XAS.

Ligand K-edge XAS data were obtained to account for the contribution of the μ_3-chalcogenide donors to the LUMO. S K-edge XAS data obtained for **3** exhibit an intense pre-edge feature at 2472.0 eV assigned by analogy to **2** as S $1s \rightarrow a_2''$ (LUMO) (Figure 5a). The intensity of this peak (D_0) was used to determine the S $3p$ contribution to a_2'' (α^2) using equation 1:

$$D_0 = \frac{\alpha^2 I_s h}{3n} \quad (1)$$

where h is the number of holes in the acceptor orbital, n is the number of degenerate photoabsorbers, and I_s is the dipole integral corresponding to a pure S $1s \rightarrow$ S $3p$ absorption. The value of I_s for **3** was estimated at 10.6 based on assignment of the S $1s \rightarrow$ S $4p$ transition at 2475.3 eV.[24] The corresponding S $3p$ contribution to a_2'' is 30.2(1)%. Se K-edge XAS data were obtained for **4**. These data show a pre-edge feature at 12,651.2 eV, which is poorly resolved from the rising edge (Figure 5b). Although these data indicate covalent bonding between the Cu_3 unit and the Se ligand, quantification of the degree of Cu–Se covalency in **4** is precluded owing to the paucity of Se K-edge data of compounds with well-defined M-Se covalency coupled with the uncertainty in the extracted pre-edge peak area owing to the overlap of the pre-edge peak with the edge itself.

Electrochemical and UV/visible/nIR spectroscopic studies.

The visible absorption spectrum of **4** as a tetrahydrofuran solution has maxima at 13377 cm^{-1} (ε = 13.9(7) × 10^3 $M^{-1}cm^{-1}$) and 29325 cm^{-1} (ε = 39(1) × 10^3 $M^{-1}cm^{-1}$) (Figure S2), the former being blue-shifted relative to that for **3** (λ_{max} = 12400 cm^{-1}). The difference between the absorption maxima of **3** and **4** agrees with the $\Delta E_{1/2}$ = 0.14 V from cyclic voltammetry measurements on **3** and **4** in THF ($E_{1/2}$ = –1.44 V and –1.58 V vs. Fc/Fc^+ for **3** and **4**, respectively) (Figure S12, S13).[14] Cyclic voltammograms of **2** are more complex than that of **3** or **4**, with a reversible one-electron process at –1.35 V vs. Fc/Fc^+ followed by two broad irreversible features at ca. –1.55 and –1.7 V (Figure S10, S11). The latter irreversible processes could arise from an ECE type mechanism, although the nature of the chemical reaction step is unclear. In contrast to the heavier chalcogen-bridged congeners, we observe only a broad feature at 7364 cm^{-1} (ε = 2470 $M^{-1}cm^{-1}$) with a shoulder at 6480 cm^{-1} in UV/vis/nIR spectra of **2** (Figure S1). The spectral features for **2** and **4** are insensitive to solvent as has been previously reported for **3**. A valence-delocalized pyrazolate-ligated $[Cu_3(\mu_3\text{–}O)]^{5+}$ cluster exhibits an asymmetric band at 9550 cm^{-1} (ε = 2600 $M^{-1}cm^{-1}$), which is attributed to an intervalence charge transfer (IVCT).[16b] This comparison suggests that the long wavelength absorptions in **2** and **4** may be IVCT in nature. As Di Francesco, et al. previously noted[14] for **3**, however, these broad bands in spectra of **2** and **4** seemingly

contraindicate canonical valence delocalization within the framework of a simplified two-state IVCT model, and are more cosistent with a charge localized state.[25] Insofar as our NMR data and UV/visible/nIR data are inconclusive regarding an assignment of the extent of charge delocalization, we employed electronic structure calculations benchmarked to our experimental data to describe the nature of the bonding interactions in these $[Cu_3E]^{3+}$ cores.

Electronic structure calculations.

Geometry optimizations were performed via both restricted Kohn-Sham (RKS) and broken-symmetry [BS(1,1)] DFT and PBE0 hybrid DFT calculations on truncated models of **2**–**4** (**2′**–**4′**) in which the ethyl substituents on the benzene rings were replaced with methyl groups. The PBE0/def2-tzvp RKS solutions yielded structures most consistent with experimental metrical parameters derived by EXAFS or XRD (Table S4). Single point calculations were then carried out (PBE0/ZORA-def2-tzvp(-f)) using the RKS coordinates. MO diagrams produced for **2**–**4** are qualitatively similar. In all cases, the LUMO is a_2'' Cu $3d_{xz/yz}$ – E $2p_z$ π*. These LUMOs and their admixture coefficients are reproduced in Figure 6. In general, there is excellent agreement between experimental and DFT-calculated Cu 3*d* contributions to this LUMO. Although S 3*p* character in the LUMO of **3** was the only ligand contribution that could be reliably quantified, this value too exhibits splendid agreement between experimental (30.2%) and calculated (33.4%) values.

The aforementioned single points were then used as starting points for XAS predictions. Typically, such calculations are restricted to metal and ligand K-edge XAS, for which TDDFT produces results in good agreement with experimental data. However, TDDFT is inadequate for the prediction of $L_{2,3}$-edge XAS because it neglects the significant influence of core hole spin-orbit coupling on these spectra. Attempts to simulate the Cu $L_{2,3}$-edge data using a ligand field multiplets (LFM) model, supplemented with a charge transfer multiplets (CTM) approximation, were unsuccessful. In contrast, DFT-ROCIS treatment of the Cu $L_{2,3}$edge spectrum of **2** using the above RKS DFT electronic structure neatly describes the data. We note that our quantitative interpretation focuses on the Cu-L_3 edge because the Cu-L_2 edge is strongly influenced by processes that cannot be accounted for using this methodology (e.g., Auger decay, etc.).

Using DFT-ROCIS, we find a satisfactory agreement between the experimental and the calculated Cu $L_{2,3}$-edge data for **2**–**4** following energy calibration. The trend in the energy observed experimentally of the main Cu L_3 lines of **2**–**4** is reproduced by DFT-ROCIS, although the calculated energies of the satellite features remain invariant for the three complexes. For **2**, there is a slight overestimation of the energy of the satellite feature found experimentally (+1.5 eV), however, the relative intensities of the main L_3 line vs. the satellite feature are reproduced nicely (Figure S14). The DFT-ROCIS calculations reveal that the main L_3 line is comprised of 24 final states while the satellite feature is comprised of 91 final states. The final states constituting the main line are almost exclusively Cu($2p_{3/2}$) → LUMO in character, while those comprising the satellite feature are admixtures of a number of Cu($2p_{3/2}$) transitions into higher lying orbitals. We find that the average Cu(3*d*) composition of the final states comprising the main line is 55.0%, whereas that of the satellite feature is 5.0%. Averaging over these states yields a total main-line to satellite

Cu(3d) ratio of ~3:1, which is in reasonable agreement with the integrated experimentally-observed main-line to satellite intensity ratio of 4.6:1. It should be noted that we have neglected intensity contributions from Cu $2p \rightarrow 4s$ excitations because, although formally allowed, we determined the $\langle 2p|4s\rangle$ overlap integral calculated for Cu in these compounds have ca. 1% the value of the corresponding $\langle 2p|3d\rangle$ overlap integral. Thus, these excitations should minimally contribute to the observed intensity. For complex **3** we find that both the main L_3 line and the satellite feature are blue shifted by +1.0 eV relative to the experimental data, while the main L_3 line and satellite feature calculated for **4** are blue shifted by +0.8 eV relative to the experimental data. As with **2**, the DFT-ROCIS calculations also over-estimate the degree of copper character to the final states (the ratio of the average Cu(3d) character to the main line:satellite feature are 49%:4.7% and 47%:5.0% for **3** and **4**, respectively). In other words, the calculated trends in final state 3d character do not display as dramatic of a decrease as those observed experimentally. However, this is to be expected because DFT-ROCIS calculations do not capture additional physical processes such as Auger emission that contribute to defining the intensities of L-edge peaks. Nevertheless, DFT-ROCIS reproduces adequately the experimentally observed trends in the experimental Cu L-edge data for these compounds.

Although TDDFT could reproduce the features of the K-edge spectra adequately, we chose to use the DFT-ROCIS method to simulate the edge regions of Cu K-edge XANES spectra for **2** for consistency (Figure 7). The pre-edge features of the Cu K-edge XANES are attributed to excitations to states that arise almost exclusively due to Cu $1s \rightarrow a_2''$ LUMO transitions. These calculations also suggest that the higher energy excitations, which are buried in the edge spectrum, are attributable to states with a high degree of multi-configurational character, and are comprised of orbitals that can be best described as transitions into states mostly comprised of Cu(4*p*) and O(2*p*) character. The DFT-ROCIS calculations also suggest that these transitions are present in the Cu Kedge XANES spectra of **3** and **4**. The DFT-ROCIS calculations yield low energy transitions best described as Cu/S(Se) $1s \rightarrow a_2''$ LUMO transitions. These transitions are ~5 fold weaker than the analogous Cu/O $1s \rightarrow a_2''$ LUMO found in **2**. This result suggests that these transitions would be too weak to observe in the experimental spectra of **3** and **4**, consistent with our experimental data. In contrast, the higher energy transitions arising from excitations into Cu(4*p*)/S(3*p*) (Se(4*p*)) states of **3** and **4** are more intense than the corresponding excitation into the Cu(4*p*)/O(2*p*) final states of **2**. These transitions calculated for **3** and **4** are also red-shifted relative to those calculated for **2**. Thus, the DFTROCIS calculated Cu K-edge X-ray absorption spectra obtained for these complexes are consistent with the experimental data.

Despite its success in describing excited states accessed by core spectroscopy, DFT-ROCIS fails to provide meaningful agreement with the NIR spectral data. DFT-ROCIS predicts the low-energy bands at ~7000 cm^{-1} found in the experimental NIR spectrum of **2** (Figure 8), but it also predicts three degenerate and one quasi-degenerate (34 cm^{-1} above the ground state) ground states, which is inconsistent with the NMR behavior of **2**. Consequently, a multireference calculation employing the spectroscopy-oriented CI (SORCI) method was carried out for **2′**. Energies and compositions of 5 singlet and 5 triplet states were calculated using a CAS(14,10) reference. The CAS(14,10) was chosen from a set of localized MOs

involved in Cu–O bonding generated from RKS DFT using the PBE0 functional. Figure 8 exhibits the satisfactory agreement of the experimental NIR spectrum with the spectrum calculated via the SORCI procedure. Through detailed interpretation of the ground and excited states from the SORCI procedure, we have achieved a self-consistent electronic structure formulation that neatly accounts for all remaining spectroscopic observables.

The averaged atomic natural orbitals (AANOs) and their occupations comprising the CAS(14,10) used by the SORCI procedure are shown in Figure S15 and arranged in order of ground state occupancy. The CAS(14,10) captures 87% of the ground singlet state references. Once again, the LUMO in the dominant (69%) ground state configuration is predicted to be a Cu_3–O a_2'' anti-bonding combination, here comprising 15.9% O $2p_z$ with 75.4% Cu $3d_{xz/yz}$. The effectively degenerate e'LUMO+1 and LUMO+2 set in the dominant ground state configuration comprise an average 11.2 % Cu $3d$ contribution. Excitation into these orbitals would give rise to $L_{2,3}$ satellite features with a 1:3.4 intensity ratio to the main lines, in reasonable agreement with the experimental value of 1:4.6(1).

The compositions and relative energies of the singlet ground state and the four singlet and five triplet excited states produced by the SORCI calculation are compiled in Table S6. Transition energies are displayed in Table S7. The intense 7364 cm^{-1} NIR band in the experimental spectrum of **2** (Figure 8, S1) is reproduced by a calculated feature near 7200 cm^{-1} principally comprising excitations to two singlet excited states, one at 7460 cm^{-1} and one at 6730 cm^{-1}. CAS(14,10) configurations describe 86% of these states, which are multiconfigurational in nature. These states are best described as electric dipole accessible ^{1}E' excited states arising due to excitations from predominantly Cu–Cu π^* e'' MOs to the Cu_3–O π^* a_2'' LUMO (Figure S15).

The ground state electronic structure that emerges is thus characterized by delocalization of electron vacancy over the 3 Cu and 1 O centers. Based on these above observations, we emphasize that a classical oxidation state formulation (e.g., $Cu^ICu^{II}_2$ and O^{2-}) is an inadequate representation of the charge distribution in **2**. This system is highly covalent in nature, with nearly equal AO contributions between copper and oxygen atoms.

Nature of the Tricopper-Chalcogen Bonds.

Based on the above analysis we find that not only S-ligated **3** and Se-ligated **4** possess covalent Cu-E^{2-} interactions, but complex **2** also displays a fairly high degree of covalent Cu-oxo bonding character. Two important insights into the copper-chalcogen interactions can be gleaned from this observation. The first is that the oxidation state formalism fails to properly describe the electronic structure of these clusters. Although it is tempting based on the absence of 1 valence electron as determined by Cu $L_{2,3}$-edge XAS to invoke a $Cu^{II}Cu^I_2$ configuration, the highly delocalized nature of the LUMO precludes such a clear-cut description. The $L_{2,3}$-edges show that ca. one 3d electron is absent from among the Cu centers, and by necessity the remaining hole character is distributed across the chalcogen and N-donors. The other noteworthy feature of this system is the fact that we find that the Cu-chalcogen bonding interactions observed in **2**–**4** are comparable to one another; the Cu-E^{2-} bond found in all three compounds display significant covalent character. The difference in electronegativities between S and Se are minimal, and thus one would predict similar

bonding interactions found in **3** and **4**. Oxygen, on the other hand, is significantly more electronegative than both S and Se. Thus, one would predict considerable difference in the bonding interactions for **2** vs. **3** and **4**, which is not observed; the bonding interactions in all three compounds follow a smooth continuum. In this homologous series of compounds, the bonding interaction observed between the chalcogens and copper are similar to the more covalent bonding one would predict for a *p*-block metal as opposed to the dative bonding scheme one would expect for transition metal complexes. This study adds to a growing body of evidence that copper occupies a unique position at the transition from the 3*d* to the *p*-block metals, with the bonding picture transitioning from a classic ligand field to highly covalent and an inverted scheme.[7–8, 11a, 12] The flexibility in bonding as a function of the coordination environment is likely a key factor in the ability of copper to perform a wide array of roles in biology, catalysis, and materials chemistry.

As mentioned above, Berry and co-workers employed spectroscopic and computational methods on a number of late transition metal dichalcogenide species, most notably $[CpNi]_2(E_2)$ and $[(TMEDA)Cu]_3(S_2)^{3+}$.[7, 26] Their consensus bonding picture is one in which ligand oxidation is preferred to metal oxidation to the Ni(III) or Cu(III) state; that is, a subsulfide, S_2^{3-}, ligand bridges the metal centers rather than a more classical ligand-field treatment with two bridging chalcogenides (e.g., two μ_3-S^{2-}) and higher metal oxidation states (e.g., $2Cu^{II}$ and $1Cu^{III}$). Their analysis evidences the strongly covalent metal-chalcogen interactions in these compounds, reminiscent of ongoing discussions regarding oxocopper(III) vs. oxylcopper(II). The covalency observed in the $[Cu_3E]^{3+}$ complexes reported here is consistent with these prior reports, with the important distinction that such covalency is observed without requiring formally copper(III) centers. Taken together, the arguments advanced by Berry and coworkers are repeated here, but are not exclusive to formally high-valent oxidation states (e.g., Cu(III) or Ni(III)) and extend to more typical oxidation states of late first row transition metals (e.g., Cu(II) or Cu(I)). Our results serve to reinforce that metal-ligand bonding in late transition metal-chalcogen species is highly covalent such that formal oxidation state assignments using classical ligand field theory fail to describe accurately the electronic structure of these systems.

Conclusions

We have presented the detailed spectroscopic and computational study of a series of trinuclear copper clusters, each possessing a covalent $[Cu_3(\mu_3–E)]^{3+}$ unit. This bonding picture synthesizes a suite of spectroscopic methods benchmarked to electronic structure calculations. Key observations are the validation by XAS and ESI/MS methods for incorporation of the interstitial oxygen, the Cu $L_{2/3}$-edge spectral analysis which revealed value 50(1)% Cu 3*d* character in the LUMO. This composition of the LUMO and the experimental nIR data were faithfully reproduced in the CAS(14,10) calculation. Across the series, the contribution of the bonding interactions between the Cu 3*d* and the chalcogen orbitals are analogous to each other. Although the degree of copper character to the LUMO decreases as one progresses from the O to the Se analogues, the 17% overall decrease is not dramatic.

Finally, we emphasize that a judicious choice of computational methods carefully benchmarked to a variety of experimental techniques is vital to obtain any valid and meaningful insight into these systems. As electronic structure calculations become increasingly accessible, it has unfortunately become accordingly more common to encounter studies showcasing the "method of the moment" without proper consideration of the underlying chemical physics. In our present example, although hybrid DFT methods were successful in reproducing the geometry of **2**, these methods failed to accurately describe several of the spectroscopic properties of **2**. Furthermore, these methods yielded a representation of the electronic structure of **2** at odds with the experimental data. In fact, we found there was no one computational approach that could reliably be applied to all aspects of this study. This study therefore highlights the importance of scrutinizing calculations used to interpret experimental results.

Experimental

General considerations.

All reactions were performed under a dinitrogen atmosphere in an Innovative Technologies glovebox. Solvents were purchased from Sigma-Aldrich, dried using an Innovative Technologies solvent purification system, and then stored over activated 3Å molecular sieves inside the dinitrogen-filled glovebox. Reagents were purchased from Sigma-Aldrich or Strem Chemicals and used as received. Deuterated solvents were purchased from Cambridge Isotope Laboratories (CIL) and purified according to reported procedures and then stored over activated 3Å molecular sieves.1 NMR spectra were collected on a Varian Inova operating at 500 MHz for ^{1}H, equipped with a 3-channel 5 mm indirect detection probe with z-axis gradients. All chemical shifts are reported in ppm, and referenced to tetramethylsilane for ^{1}H. ^{31}P NMR spectra were measured on a Bruker Mercury operating at 300 MHz for ^{1}H. Electrospray ionization (ESI) mass spectra were collected in positive mode by direct injection using a manual injector which fed into a constant flow of anhydrous air-free solvent, and then into an Agilent 6120 TOF spectrometer. The following ESI and MS conditions were used: gas temperature = 350 ˚C, and fragmentation voltage = 120 V. UV/visible spectra were recorded on a Hewlett-Packard 8453 UVvisible spectrophotometer in anhydrous benzene, and UV/vis/nIR spectra were recorded on a Perkin Elmer Lambda 900 double path spectrophotometer in anhydrous benzene using quartz cuvettes having airfree screw top seal (Starna Cells Inc., Atascadero, CA, USA). The ligand, H_3**L**,[27] and tricopper complex, **1**,[20] were synthesized as reported previously. Iodosobenzene was synthesized as described elsewhere.[28]

Cyclic Voltammetry experiments were performed in a nitrogen atmosphere glovebox using a Princeton Applied Research Versastat II potentiostat and a three-electrode setup (3 mm Pt button working, Au wire counter, and Ag/AgCl reference) with electrodes purchased from BASi, Inc. and/or CH Instruments, Inc.

S K-edge XAS data were obtained at SSRL beamline 4−3 under ring conditions of 3 GeV and 500 mA. Samples were prepared by grinding to a fine powder and were spread to a vanishing thickness onto 38 μm low-S Mylar tape. All samples were measured in a He atmosphere at room temperature in fluorescence mode using a Lytle detector. The incident

beam energy was calibrated by setting the energy of the first peak in the S Kedge spectrum of $Na_2S_2O_3{\cdot}5H_2O$ to 2472.02 eV. Intensity was normalized with respect to the incident beam using a He-filled ion chamber upstream of the sample. Data represent an average of three scans measured from 2400 to 2800 eV. Data were processed with SIXPACK.[29] Spectra were normalized by fitting a polynomial flattened to energies below 2490 eV to the data and normalizing the region below 2490 eV to unity.

Synthesis of Cu_3OL (2).

The following procedure is a representative example. A solution of $Cu_3(N_2)$**L** (200 mg, 0.220 mmol) in toluene (~ 15 mL) at 100 ˚C was added to a vial containing yellow iodosobenzene (70.0 mg, 0.318 mmol). The reaction was maintained at 100 ˚C with vigorous stirring for 5 min, during which the deep red solution became dark greenish-yellow in appearance. The reaction mixture was then quickly filtered through a Celite plug, which was pre-rinsed with hot toluene. The solvent was removed under reduced pressure. The residue was ground to a fine powder and further dried at 100 ˚C under vacuum for 2 h to remove residual iodobenzene. Dissolution of the residue in benzene followed by lyophilization of the solvent affords the product as a free flowing powder (185 mg, 94%). For synthesis using trimethylamine *N*oxide, the reaction was performed at room temperature over the course of 24 h and the product isolated in comparable yield as described above. **IR (cm^{-1}):** 2956, 1536, 1469, 1407, 1014, 730. **^{1}H NMR (300 MHz, $d_8$toluene, 298 K)** ppm: 1.47 (t, *J*=7.33 Hz, 6 H) 1.88 (s, 18 H) 3.18 (q, *J*=7.33 Hz, 12 H) 4.01 (s, 12 H) 4.50 (s, 3 H). **^{13}C NMR(101 MHz, C_6D_6, 298 K):** δ(ppm) 163.1, 141.2, 96.4, 49.4, 23.6, 23.0, 17.2. **HRMS (ESI-TOF) *m/z*:** $[M]^+$ Calculated 894.2935 for $C_{45}H_{63}N_6Cu_3O$; $[M+H]^+$ 895.3014 Calculated $C_{45}H_{64}N_6Cu_3O$, Found 895.3020.

Synthesis of Cu_3SL (3).

The procedure used is a modified version of the previous report.[14] A 20 mL scintillation vial was charged with $Cu_3(N_2)$**L** (300 mg, 0.336 mmol) and toluene (~ 15 mL). This vial was heated to 100 ˚C. S_8 (25 mg, 0.781 mmol) was added to a separate 20 mL vial equipped with PTFE magnetic stir bar. The hot toluene solution of **1** was rapidly added to the stirring the vial containing S_8 and the reaction maintained at 100 ˚C. Upon mixing, the reaction mixture evolved to an emerald green mixture. The reaction was stirred at 100 ˚C for 5 min, then rapidly filtered through pre-rinsed Celite while hot through a ground glass fritted funnel (fine porosity) packed with Celite and the green filtrate collected. Volatiles were removed under reduced pressure to yield a microcrystalline green solid. Dissolution in benzene and subsequent lyophilization of a frozen benzene solution under reduced pressure yielded **2** as spectroscopically pure green powder (145 mg, 48%). NMR, IR, and ESI/MS data are indistinguishable from that reported previously.

Synthesis of Cu_3SeL (4).

The synthesis was carried as for **3** with the following modifications. After mixing the preheated solution of $Cu_3(N_2)$**L** (300 mg, 0.336 mmol) in toluene (~15 mL) with Se metal (60 mg, 0.760 mmol), the reaction mixture was allowed to stir at 100 ˚C for 2 h, over which time a gradual color change from dark red to dark green was observed. The work-up was as

for **3**, yielding the selenide congener, **4**, as a forest green powder (270 mg, 86%). Single crystals suitable for X-ray diffraction were obtained from slow evaporation of a saturated benzene solution at 25°C. **IR(cm^{-1}):** 2959, 1524, 1404, 1329, 1012. **^{1}H NMR (500 MHz, C_6D_6, 298 K):** δ (ppm) 4.97 (s, 3H, C**H**), 4.51 (s, 12H, N-C**H$_2$**), 2.70 (q, $^{3}J_{H-H}$ = 7.5 Hz, 12H, CH_2CH$_3$), 2.07 (s, 18H, CC**H$_3$**), 1.14(t, $^{3}J_{H-H}$ = 7.5 Hz, 18H, CH$_2$C**H$_3$**). **^{13}C NMR (101 MHz, d8-toluene, 298 K):** δ(ppm) 164.4, 143.7, 138.1, 98.0, 50.8, 23.1, 22.4, 16.5. **HRMS (ESI-TOF)** *m*/*z*: $[M+H]^+$ 959.2233 Calculated $C_{45}H_{64}N_6Cu_3Se$, Found 959.2256

Reactivity studies of 2.

An analogous procedure was employed for trimethylphosphine, tris-*tert*-butylphosphine, triphenylphosphine, dihydroanthracene, 2,6-di-*tert*-butylphenol, xanthene, styrene, cyclohexene, and ethylmethylsulfide, with the exception of propylene. Ethylmethyl sulfide (0.8 μL, 9 μmol) and **2** (3.0 mg, 3.3 μmol) were dissolved in $d_6$benzene (~0.4 mL) in an NMR tube, and then removed from the glovebox. ^{1}H- or ^{31}P-NMR spectra were then recorded after 30 min and 24 h. For propylene, **2** (3.0 mg, 3.3 μmol) was dissolved in d_6-benzene (~0.4 mL) in a J-Young NMR tube, and then transferred to a vacuum manifold. A freeze-pump-thaw cycle was then carried out on the sample, after which the tube was refilled with propylene to ~1 atm. ^{1}H-NMR spectra were recorded as noted for other substrates.

Copper and Selenium K-edge X-ray Absorption Spectroscopy.

Solid samples of Cu_3O**L**, Cu_3Se**L**, and $Cu_3(N_2)$**L** were finely ground in boron nitride and placed into 1 mm aluminum samples holders between 37 μm Kapton tape windows. Data were obtained in transmission mode using N_2 filled ionization chambers on beamline 2–2 at the Stanford Synchrotron Radiation Light Source (SSRL) under ring conditions of 3 GeV and 500 mA. Light was monochromated using a Si(111) double monochromator, which was detuned 40% to eliminate higher order harmonics. Samples were maintained at 20 K throughout data collection with the use of a He Displex closed cycle cryostat.

For the Cu K-edge data, spectra were calibrated against the simultaneously recorded spectrum of a Cu foil standard with the first inflection point set to 8980.3 eV. The monochromator position displayed no perceptible drift during data analysis, with the resulting measured energy difference being < 0.1 eV from spectrum to spectrum. XANES data were obtained in 10 eV steps in the pre-edge region (8779 – 8969 eV), 0.3 eV steps in the edge region (8969 – 8999 eV), and 0.5 eV in the near edge region (8999 – 9129 eV). Each data set represents the sum of 3 individual data sets. EXAFS data were collected in 10 eV steps in the pre-edge region (8779 – 8969 eV), 0.5 eV steps in the edge region (8969 – 8989 eV), 1 eV in the near edge region (8989 – 9009 eV), and 0.05 k steps in the far edge region (9009 – 16.5 *k*). Data were worked-up and analyzed using the XAS analysis package *EXAFS123*.[30] Prior to baseline fitting all know monochromator glitches were removed from the X-ray absorption spectra. The pre-edge background was removed from the averaged spectra by fitting the pre-edge region to a polynomial function. The background in the EXAFS region was fit to a third order spline function. EXAFS data were modeled using the single scatter approximation using phase and amplitude files generated with *FEFF v 8.2* as previously described.[31]

For Se K-edge data, spectra were calibrated against the simultaneously recorded spectrum of an elemental Se standard with the first inflection point set to 12658 eV. Data were obtained in 10 eV steps in the pre-edge region (12458 – 12645 eV), 0.3 eV steps in the edge region (12645 – 12678 eV), and 0.5 eV (12678 eV – 12758 eV). Data were then processed as outlined above.

Soft X-ray Absorption Spectroscopy.

A solid sample of Cu_3O**L** was spread onto conductive carbon tape mounted on an aluminum sample rod. Cu $L_{2,3}$-edge XAS data were collected at the Stanford Synchrotron Radiation Lightsource (SSRL) at beamline 10–1 under ring conditions of 3 GeV and 500 mA. Data were collected in fluorescence mode. 4 scans were measured from 910 to 975 eV, each normalized to incident x-ray flux as measured using the photocurrent of a gold grid reference monitor, and these scans were averaged and processed using PyMCA. For both Cu $L_{2,3}$ XAS, the pre-edge background was removed from the averaged spectrum by fitting a linear fit to the pre-edge region (Cu: 920–925 eV) and subtracting this line from the entire spectrum. A linear spline was fit from 965 to 975 eV and this line was subtracted from the data, which were then normalized to a value of 1.0 at 965 eV. For Cu $L_{2,3}$, energy was calibrated using published values for the L_3 and L_2 peaks of CuF_2 at 930.5 and 950.5 eV. Cu CuF_2 was measured before and after data collection, and averaged values were used for the calibration.

Electronic Structure Calculations.

Electronic structure calculations were performed using the software package *ORCA v. 3.03*.[32] DFT were performed using the def2-tzvp basis set on all atoms and the atom pairwise dispersion correction with Becke-Johnson damping to account for dispersive interactions.[33] ORCA VeryTightSCF convergence criteria were used for the SCF cycles, with program defaults used for all other convergence criteria and settings.[32] Both restricted closed shell and broken symmetry solutions were considered. Geometry optimizations were performed at the BP86 level,[34] and used the RI approximation and def2tzvp/c auxiliary basis set.[35] Single point calculations were performed at the PBE0 level[36] and used the RIJCOSX approximation and def2-tzvp/j auxiliary basis set.[37] For calculation of the X-ray absorption spectra both BS and RKS solutions were utilized at the PBE0 level. Each yielded good agreement with the experimental data. Calculations employed the def2tzvp(-f) basis set and the ZORA approximation.[33b, 38] Cu K and $L_{2,3}$-edge XAS were calculated using DFT-ROCIS.[39] For each Cu $L_{2,3}$-edge calculation and the Cu K edge calculations, the first 50 roots were examined. The DFT-ROCIS employed Coulomb ($c_1 = 0.21$) exchange ($c_2 = 0.49$) and off-diagonal CI matrix scaling parameters ($c_3 = 0.29$) previously defined for the B3LYP functional. Cu K-edge spectra were simulated by employing a –4.6 eV shift to all transitions, applying a Gaussian line shape to each transition (FWHM = 1.3 eV), and summing each individual transition. Cu L-edge spectra were simulated by employing a +7.6 eV shift to all transitions, applying a Gaussian line shape to each transition (FWHM = 1.0 eV), and summing each individual transition.

Multireference character in the ground state of **2** was assessed with SORCI[40] calculations. SORCI was performed on a complete active space (CAS) for truncated 2 (Cu_3O**L**$^{\mathbf{Me}}$)

comprising 10 electrons and 8 orbitals [CAS(14,10)]. The def2-SVP-ZORA basis set was used on all atoms except for hydrogens, for which the MINIX basis was used.[41] The ZORA relativistic correction was used in all SORCI calculations. As described elsewhere,[40] individual selection was used to ease the computational burden. The size of the first-order interacting space was reduced with a threshold: $T_{sel} = 10^{-6}$ E_h. A further approximation involved reducing the reference space through another selection: all initial references that contributed less than a second threshold ($T_{pre} = 10^{-5}$) to the zerothorder states were rejected from the reference space. Starting orbitals were taken from restricted Kohn–Sham (RKS) orbitals generated via a PBE0 calculation.

Supplementary Material

Refer to Web version on PubMed Central for supplementary material.

ACKNOWLEDGMENT

The authors graciously acknowledge support from the following: National Science Foundation CAREER CHE-1454455 (KML), CHE1464876 (LJM), CHE-1048604 (UF), and CHE-1565766 (JS), and 52704-DNI3 (LJM); National Institutes of Health: R15-GM120641–01 (JS); Alfred P. Sloan Foundation (KML). R.B.F was supported by a University of Florida Graduate Research Fellowship. LJM thanks Prof J. Gardinier for acquiring nIR spectra. XAS data were obtained at SSRL, which is supported by the U.S. Department of Energy, Office of Science, Office of Basic Energy Sciences under Contract No. DE-AC0276SF00515. The SSRL Structural Molecular Biology Program is supported by the Department of Energy's Office of Biological and Environmental Research, and by NIH/NIGMS (including P41GM103393).

ABBREVIATIONS

XAS	X-ray Absorption Spectroscopy
XANES	X-ray Absorption NearEdge Spectroscopy
EXAFS	Extended X-ray Absorption Fine Structure
NMR	Nuclear Magnetic Resonance
DFT	Density Functional Theory
ROCIS	Restricted Open-shell Configuration Interaction Singles
SORCI	Spectroscopy-Oriented Configurational Interaction

REFERENCES

1 (a). Xia Z; Fang H; Zhang X; Molokeev MS; Gautier R; Yan Q; Wei S-H; Poeppelmeier KR, CsCu5Se3: A Copper-Rich Ternary Chalcogenide Semiconductor with Nearly Direct Band Gap for Photovoltaic Application. Chem. Mater 2018;(b)Coughlan C; Ibáñez M; Dobrozhan O; Singh A; Cabot A; Ryan KM, Compound Copper Chalcogenide Nanocrystals. Chem. Rev 2017, 117 (9), 5865–6109. [PubMed: 28394585]

2 (a). Singh A; Singh S; Levcenko S; Unold T; Laffir F; Ryan KM, Compositionally Tunable Photoluminescence Emission in Cu2ZnSn(S1−xSex)4 Nanocrystals. Angew. Chem. Int. Ed 2013, 52 (35), 9120–9124;(b)Comin A; Manna L, New Materials for Tunable Plasmonic Colloidal Nanocrystals. Chem. Soc. Rev 2014, 43 (11), 3957–3975; [PubMed: 24435209] (c)Niezgoda JS; Rosenthal SJ, Synthetic Strategies for Semiconductor Nanocrystals Expressing Localized Surface Plasmon Resonance. ChemPhysChem 2016, 17 (5), 645–653; [PubMed: 26530667]

(d)Willhammar T; Sentosun K; Mourdikoudis S; Goris B; Kurttepeli M; Bercx M; Lamoen D; Partoens B; Pastoriza-Santos I; Pérez-Juste J; Liz-Marzán LM; Bals S; Van Tendeloo G, Structure and Vacancy Distribution in Copper Telluride Nanoparticles Influence Plasmonic Activity in the Near-Infrared. Nat. Commun 2017, 8, 14925; [PubMed: 28358039] (e)Kriegel I; Jiang C; Rodríguez-Fernández J; Schaller RD; Talapin DV; da Como E; Feldmann J, Tuning the Excitonic and Plasmonic Properties of Copper Chalcogenide Nanocrystals. J. Am. Chem. Soc 2012, 134 (3), 1583–1590; [PubMed: 22148506] (f)Kriegel I; Rodríguez-Fernández J; Wisnet A; Zhang H; Waurisch C; Eychmüller A; Dubavik A; Govorov AO; Feldmann J, Shedding Light on Vacancy-Doped Copper Chalcogenides: Shape-Controlled Synthesis, Optical Properties, and Modeling of Copper Telluride Nanocrystals with Near-Infrared Plasmon Resonances. ACS Nano 2013, 7 (5), 4367–4377; [PubMed: 23570329] (g)Llorente VB; Dzhagan VM; Gaponik N; Iglesias RA; Zahn DRT; Lesnyak V, Electrochemical Tuning of Localized Surface Plasmon Resonance in Copper Chalcogenide Nanocrystals. J. Phys. Chem. C 2017, 121 (33), 18244–18253.

3 (a). Kashida S; Shimosaka W; Mori M; Yoshimura D, Valence Band Photoemission Study of the Copper Chalcogenide Compounds, Cu2S, Cu2Se and Cu2Te. J. Phys. Chem. Solids 2003, 64 (12), 2357–2363;(b)Davletshina AD; Yakshibaev RA; Bikkulova NN; Stepanov YM; Bikkulova LV, Ab initio Calculations of Band Structure of Solid Solutions of Copper and Silver Chalcogenides. Solid State Ionics 2014, 257, 29–31;(c)Ghosh A; Biswas A; Thangavel R; Udayabhanu G, Photo-Electrochemical Properties and Electronic Band Structure of Kesterite Copper Chalcogenide Cu2-II-Sn-S4 (II = Fe, Co, Ni) thin films. RSC Adv. 2016, 6 (98), 96025–96034.

4. Grundner S; Markovits MAC; Li G; Tromp M; Pidko EA; Hensen EJM; Jentys A; Sanchez-Sanchez M; Lercher JA, Single-Site Trinuclear Copper Oxygen Clusters in Mordenite for Selective Conversion of Methane to Methanol. Nat. Commun 2015, 6, 7546. [PubMed: 26109507]

5. Brown EC; York JT; Antholine WE; Ruiz E; Alvarez S; Tolman WB, [Cu3(μ-S)2]3+ Clusters Supported by N-Donor Ligands: Progress Toward a Synthetic Model of the Catalytic Site of Nitrous Oxide Reductase. J. Am. Chem. Soc 2005, 127, 13752–13753. [PubMed: 16201771]

6(a). Elwell CE; Gagnon NL; Neisen BD; Dhar D; Spaeth AD; Yee GM; Tolman WB, Copper–Oxygen Complexes Revisited: Structures, Spectroscopy, and Reactivity. Chem. Rev 2017, 117, 2059–2107; [PubMed: 28103018] (b)Vanelderen P; Snyder BER; Tsai ML; Hadt RG; Vancauwenbergh J; Coussens O; Schoonheydt RA; Sels BF; Solomon EI, Spectroscopic Definition of the Copper Active Sites in Mordenite: Selective Methane Oxidation. J. Am. Chem. Soc 2015, 137 (19), 6383–6392; [PubMed: 25914019] (c)Woertink JS; Smeets PJ; Groothaert MH; Vance MA; Sels BF; Schoonheydt RA; Solomon EI, A [Cu2O]2+ Core in Cu-ZSM-5, the Active Site in the Oxidation of Methane to Methanol. Proc. Natl. Acad. Sci. U. S. A 2009, 106 (45), 18908–18913; [PubMed: 19864626] (d)Kim S; Stahlberg J; Sandgren M; Paton RS; Beckham GT, Quantum Mechanical Calculations Suggest that Lytic Polysaccharide Monooxygenases use a Copper-Oxyl, Oxygen-Rebound Mechanism. Proc. Natl. Acad. Sci. U. S. A 2014, 111 (1), 149–154; [PubMed: 24344312] (e)Lewis EA; Tolman WB, Reactivity of Dioxygen−Copper Systems. Chem. Rev 2004, 104, 1047–1076. [PubMed: 14871149]

7. Berry JF, Two-Center/Three-Electron Sigma Half-Bonds in Main Group and Transition Metal Chemistry. Acc. Chem. Res 2016, 49 (1), 27–34. [PubMed: 26741459]

8. Sarangi R; Yang L; Winikoff SG; Gagliardi L; Cramer CJ; Tolman WB; Solomon EI, X-ray Absorption Spectroscopic and Computational Investigation of a Possible S…S Interaction in the [Cu3S2]3+ Core. J. Am. Chem. Soc 2011, 133 (43), 17180–17191. [PubMed: 21923178]

9 (a). Himes RA; Karlin KD, A New Copper-Oxo Player in Methane Oxidation. Proc. Natl. Acad. Sci. U. S. A 2009, 106 (45), 18877–18878; [PubMed: 19889982] (b)Lee JY; Karlin KD, Elaboration of Copper– Oxygen Mediated C–H Activation Chemistry in Consideration of Future Fuel and Feedstock Generation. Curr. Opin. Chem. Biol 2015, 25, 184–193; [PubMed: 25756327] (c)Solomon EI; Heppner DE; Johnston EM; Ginsbach JW; Cirera J; Qayyum M; Kieber-Emmons MT; Kjaergaard CH; Hadt RG; Tian L, Copper Active Sites in Biology. Chem. Rev 2014.

10 (a). Donoghue PJ; Tehranchi J; Cramer CJ; Sarangi R; Solomon EI; Tolman WB, Rapid C-H Bond Activation by a Monocopper(III)-Hydroxide Complex. J. Am. Chem. Soc 2011, 133 (44), 17602–17605; [PubMed: 22004091] (b)Dhar D; Yee GM; Spaeth AD; Boyce DW; Zhang H; Dereli B; Cramer CJ; Tolman WB, Perturbing the Copper(III)-Hydroxide Unit through Ligand Structural

Variation. J. Am. Chem. Soc 2016, 138 (1), 356–368; [PubMed: 26693733] (c)Dhar D; Tolman WB, Hydrogen Atom Abstraction from Hydrocarbons by a Copper(III)Hydroxide Complex. J. Am. Chem. Soc 2015, 137 (3), 1322–1329. [PubMed: 25581555]

11 (a). Walroth RC; Lukens JT; MacMillan SN; Finkelstein KD; Lancaster KM, Spectroscopic Evidence for a 3d(10) Ground State Electronic Configuration and Ligand Field Inversion in [Cu(CF3)4]1-. J. Am. Chem. Soc 2016, 138 (6), 1922–1931; [PubMed: 26844693] (b)Tomson NC; Williams KD; Dai X; Sproules S; DeBeer S; Warren TH; Wieghardt K, Re-Evaluating the Cu K Pre-Edge XAS Transition in Complexes with Covalent Metal–Ligand Interactions. Chem. Sci 2015, 6 (4), 2474–2487. [PubMed: 29308158]

12. Hoffmann R; Alvarez S; Mealli C; Falceto A; Cahill TJ; Zeng T; Manca G, From Widely Accepted Concepts in Coordination Chemistry to Inverted Ligand Fields. Chem. Rev 2016, 116 (14), 8173–8192. [PubMed: 27398715]

13 (a). Bakhoda A; Jiang Q; Bertke JA; Cundari TR; Warren TH, Elusive Terminal Copper Arylnitrene Intermediates. Angew. Chem. Int. Ed 2017, 56 (23), 6426–6430;(b)Aguila MJB; Badiei YM; Warren TH, Mechanistic Insights into C–H Amination via Dicopper Nitrenes. J. Am. Chem. Soc 2013, 135 (25), 9399–9406; [PubMed: 23656170] (c)King ER; Hennessy ET; Betley TA, Catalytic C−H Bond Amination from High-Spin Iron Imido Complexes. J. Am. Chem. Soc 2011, 133 (13), 4917–4923; [PubMed: 21405138] (d)Wilding MJT; Iovan DA; Betley TA, High-Spin Iron Imido Complexes Competent for C–H Bond Amination. J. Am. Chem. Soc 2017, 139 (34), 12043–12049; [PubMed: 28777558] (e)Wilding MJT; Iovan DA; Wrobel AT; Lukens JT; MacMillan SN; Lancaster KM; Betley TA, Direct Comparison of C–H Bond Amination Efficacy through Manipulation of Nitrogen-Valence Centered Redox: Imido versus Iminyl. J. Am. Chem. Soc 2017, 139 (41), 14757–14766. [PubMed: 28937756]

14. Di Francesco GN; Gaillard A; Ghiviriga I; Abboud KA; Murray LJ, Modeling Biological Copper Clusters: Synthesis of a Tricopper Complex, and Its Chloride- and Sulfide-Bridged Congeners. Inorg. Chem 2014, 53 (9), 4647–4654. [PubMed: 24745804]

15 (a). Johnson BJ; Antholine WE; Lindeman SV; Graham MJ; Mankad NP, A One-Hole Cu4S Cluster with N2O Reductase Activity: A Structural and Functional Model for CuZ*. J. Am. Chem. Soc 2016, 138 (40), 13107–13110;(b)Zhai J; Filatov AS; Hillhouse GL; Hopkins MD, Synthesis, Structure, and Reactions of a Copper-Sulfido Cluster Comprised of the Parent Cu2S Unit: {(NHC)Cu}2(μ-S). Chem. Sci 2016, 7 (1), 589–595; [PubMed: 28791108] (c)Bagherzadeh S; Mankad NP, Oxidation of a [Cu2S] Complex by N2O and CO2: Insights into a Role of Tetranuclearity in the CuZ Site of Nitrous Oxide Reductase. Chem. Commun 2018, 54 (9), 1097–1100;(d)Zhai J; Hopkins MD; Hillhouse GL, Synthesis and Structure of a CuI3S Cluster Unsupported by Other Bridging Ligands. Organometallics 2015, 34 (19), 4637–4640.

16. (a) Rivera-Carrillo M; Chakraborty I; Mezei G; Webster RD; Raptis RG, Tuning of the [Cu3(μ-O)]4+/5+ Redox Couple: Spectroscopic Evidence Charge Delocalization in the Mixed-Valent [Cu3(μ-O)]5+ Species. Inorg. Chem 2008, 47 (17), 7644–7650; [PubMed: 18680363] (b)Mezei G; McGrady JE; Raptis RG, First Structural Characterization of a Delocalized, Mixed-Valent, Triangular Cu37+ Species: Chemical and Electrochemical Oxidation of a Cu3II(μ3-O) Pyrazolate and Electronic Structure of the Oxidation Product. Inorg. Chem 2005, 44 (21), 7271–7273; [PubMed: 16212340] (c)Suh MP; Han MY; Lee JH; Min KS; Hyeon C, One-Pot Template Synthesis and Properties of a Molecular Bowl: Dodecaaza Macrotetracycle with μ3-oxo and μ3Hydroxo Tricopper(II) Cores. J. Am. Chem. Soc 1998, 120 (15), 3819–3820.

17. Heppner DE; Kjaergaard CH; Solomon EI, Mechanism of the Reduction of the Native Intermediate in the Multicopper Oxidases: Insights into Rapid Intramolecular Electron Transfer in Turnover. J. Am. Chem. Soc 2014, 136 (51), 17788–17801. [PubMed: 25490729]

18 (a). (Li B; Li J; Liu R; Zhu H; Roesky HW, Facile Route to Rare Heterobimetallic Aluminum–Copper and Aluminum–Zinc Selenide Clusters. Inorg. Chem 2017, 56 (6), 3136–3139; [PubMed: 28267313] (b)Kimani MM; Brumaghim JL; VanDerveer D, Probing the Antioxidant Action of Selenium and Sulfur Using Cu(I)-Chalcogenone Tris(pyrazolyl)methane and -borate Complexes. Inorg. Chem 2010, 49 (20), 9200–9211; [PubMed: 20836514] (c)Azizpoor Fard M; Levchenko TI; Cadogan C; Humenny WJ; Corrigan JF, Stable -ESiMe3 Complexes of CuI and AgI (E=S, Se) with NHCs: Synthons in Ternary Nanocluster Assembly. Chem. Eur. J 2016, 22 (13), 4543–4550; [PubMed: 26865473] (d)Tan G; Xiong Y; Inoue S; Enthaler S; Blom B; Epping JD; Driess

M, From Elusive Thio- and Selenosilanoic Acids to Copper(I) Complexes with Intermolecular Si=E → Cu-O-Si Coordination Modes (E = S, Se). Chem. Commun 2013, 49 (49), 5595–5597.

19. Kau LS; Spira-Solomon DJ; Penner-Hahn JE; Hodgson KO; Solomon EI, X-ray Absorption Edge Determination of the Oxidation State and Coordination Number of Copper. Application to the Type 3 site in Rhus Vernicifera Laccase and its Reaction with Oxygen. J. Am. Chem. Soc 1987, 109 (21), 6433–6442.
20. Murray LJ; Weare WW; Shearer J; Mitchell AD; Abboud KA, Isolation of a (Dinitrogen)Tricopper(I) Complex. J. Am. Chem. Soc 2014, 136 (39), 13502–13505. [PubMed: 25238198]
21. Sarangi R; Aboelella N; Fujisawa K; Tolman WB; Hedman B; Hodgson KO; Solomon EI, X-ray Absorption Edge Spectroscopy and Computational Studies on LCuO2 Species: Superoxide−CuII versus Peroxide−CuIII Bonding. J. Am. Chem. Soc 2006, 128 (25), 8286–8296. [PubMed: 16787093]
22. Walroth RC; Uebler JW; Lancaster KM, Probing CuI in Homogeneous Catalysis using High-Energy-Resolution Fluorescence-Detected X-ray Absorption Spectroscopy. Chem. Commun 2015, 51 (48), 9864–9867.
23 (a). DuBois JL; Mukherjee P; Stack TDP; Hedman B; Solomon EI; Hodgson KO, A systematic K-edge X-ray Absorption Spectroscopic Study of Cu(III) Sites. J. Am. Chem. Soc 2000, 122 (24), 5775–5787;(b)George SJ; Lowery MD; Solomon EI; Cramer SP, Copper L-edge Spectral Studies: A Direct Experimental Probe of the Ground-State Covalency in the Blue Copper Site in Plastocyanin. J. Am. Chem. Soc 1993, 115 (7), 2968–2969.
24. Sarangi R; DeBeer George S; Rudd DJ; Szilagyi RK; Ribas X; Rovira C; Almeida M; Hodgson KO; Hedman B; Solomon EI, Sulfur K-Edge X-ray Absorption Spectroscopy as a Probe of Ligand −Metal Bond Covalency: Metal vs Ligand Oxidation in Copper and Nickel Dithiolene Complexes. J. Am. Chem. Soc 2007, 129 (8), 2316–2326. [PubMed: 17269767]
25. D'Alessandro DM; Keene FR, Current Trends and Future Challenges in the Experimental, Theoretical and Computational Analysis of Intervalence Charge Transfer (IVCT) Transitions. Chem. Soc. Rev 2006, 35 (5), 424–440. [PubMed: 16636726]
26 (a). Yao SA; Lancaster KM; Götz AW; DeBeer S; Berry JF, X-ray Absorption Spectroscopic, Crystallographic, Theoretical (DFT) and Chemical Evidence for a Chalcogen–Chalcogen Two-Center/Three-Electron Half Bond in an Unprecedented “Subselenide” Se23− Ligand. Chem. Eur. J 2012, 18 (30), 9179–9183; [PubMed: 22730046] (b)Berry JF, A Definitive Answer to a Bonding Quandary? The Role of One-Electron Resonance Structures in the Bonding of a {Cu3S2}3+ Core. Chem. Eur. J 2010, 16 (9), 2719–2724; [PubMed: 20140913] (c)Yao SA; Martin-Diaconescu V; Infante I; Lancaster KM; Götz AW; DeBeer S; Berry JF, Electronic Structure of Ni2E2 Complexes (E = S, Se, Te) and a Global Analysis of M2E2 Compounds: A Case for Quantized E2n− Oxidation Levels with n = 2, 3, or 4. J. Am. Chem. Soc 2015, 137 (15), 4993–5011. [PubMed: 25797853]
27. Guillet GL; Sloane FT; Ermert DM; Calkins MW; Peprah MK; Knowles ES; Cizmar E; Abboud KA; Meisel MW; Murray LJ, Preorganized Assembly of Three Iron(II) or Manganese(II) μ-diketiminate Complexes Using a Cyclophane Ligand. Chem. Commun. 2013, 49 (59), 6635–6637.
28. Moriarty RMK, Jerome W, II; Zhdankin Viktor V.; Christine Courillon; Emmanuel Lacote; Max Malacria; Benjamin Darses; Philippe Dauban, Iodosylbenzene. In e-EROS Encyclopedia of Reagents for Organic Synthesis, John Wiley and Sons: 2012; pp 1–17.
29. Webb SM, SIXpack: a graphical user interface for XAS analysis using IFEFFIT. Phys. Scr 2005, 2005 (T115), 1011.
30. Shearer JS, S. R EXAFS123: A Software Package for the Work-up, Analysis and Plotting of X-ray Absorption Data., University of Nevada: Reno, 2007.
31 (a). Ankudinov AL; Bouldin CE; Rehr JJ; Sims J; Hung H, Parallel Calculation of Electron Multiple Scattering Using Lanczos Algorithms. Phys. Rev. B 2002, 65 (10), 104107; (b)Ankudinov AL; Ravel B; Rehr JJ; Conradson SD, Real-Space Multiple-Scattering Calculation and Interpretation of X-ray-Absorption Near-Edge Structure. Phys. Rev. B 1998, 58 (12), 7565–7576.
32. Neese F, The ORCA program system. WIRES Comput. Mol. Sci 2012, 2 (1), 73–78.

33 (a). Grimme S; Ehrlich S; Goerigk L, Effect of the Damping Function in Dispersion Corrected Density Functional Theory. *J. Comp. Chem*. 2011, 32 (7), 1456–1465; [PubMed: 21370243] (b)Weigend F; Ahlrichs R, Balanced Basis sets of Split Valence, Triple Zeta Valence and Quadruple Zeta Valence Quality for H to Rn: Design and Assessment of Accuracy. Phys. Chem. Chem. Phys 2005, 7 (18), 3297–3305. [PubMed: 16240044]

34. Becke AD, Density-Functional Exchange-Energy Approximation with Correct Asymptotic Behavior. Phys. Rev. A 1988, 38 (6), 3098–3100.

35. Stoychev GL; Auer AA; Neese F, Automatic Generation of Auxiliary Basis Sets. J. Chem. Theory Comput. 2017, 13 (2), 554–562. [PubMed: 28005364]

36. Perdew JP; Ernzerhof M; Burke K, Rationale for Mixing Exact Exchange with Density Functional Approximations. J. Chem. Phys 1996, 105 (22), 9982–9985.

37 (a). Adamo C; Barone V, Toward Reliable Density Functional Methods Without Adjustable Parameters: The PBE0 model. J. Chem. Phys 1999, 110 (13), 6158–6170;(b)Neese F; Wennmohs F; Hansen A, Efficient and Accurate Local Approximations to Coupled-Electron Pair Approaches: An Attempt to Revive the Pair Natural Orbital Method. J. Chem. Phys 2009, 130 (11), 114108; [PubMed: 19317532] (c)Izsák R; Neese F, An Overlap Fitted Chain of Spheres Exchange Method. J. Chem. Phys 2011, 135 (14), 144105. [PubMed: 22010696]

38 (a). Autschbach J; Ziegler T, Nuclear Spin–Spin Coupling Constants from Regular Approximate Relativistic Density Functional Calculations. I. Formalism and Scalar Relativistic Results for Heavy Metal Compounds. J. Chem. Phys 2000, 113 (3), 936–947;(b)Autschbach J; Ziegler T, Nuclear Spin–Spin Coupling Constants from Regular Approximate Relativistic Density Functional Calculations. II. Spin–Orbit Coupling Effects and Anisotropies. J. Chem. Phys 2000, 113 (21), 9410–9418;(c)Autschbach J, Two-Component Relativistic Hybrid Density Functional Computations of Nuclear Spin-Spin Coupling Tensors Using Slater-Type Basis Sets and Density-Fitting Techniques. J. Chem. Phys 2008, 129 (9), 094105; [PubMed: 19044863] (d)Autschbach J, Erratum: Two-Component Relativistic Hybrid Density Functional Computations of Nuclear Spin-Spin Coupling Tensors Using Slater-Type Basis Sets and Density-Fitting Techniques J. Chem. Phys. 129, 094105 (2008)]. J. Chem. Phys 2009, 130 (20), 209901;(e)Autschbach J, Magnitude of Finite-Nucleus-Size Effects in Relativistic Density Functional Computations of Indirect NMR Nuclear Spin–Spin Coupling Constants. ChemPhysChem 2009, 10 (13), 2274–2283. [PubMed: 19670399]

39 (a). Maganas D; Roemelt M; Havecker M; Trunschke A; Knop-Gericke A; Schlogl R; Neese F, First Principles Calculations of the Structure and V L-edge X-ray Absorption Spectra of V2O5 Using Local Pair Natural Orbital Coupled Cluster Theory and Spin-Orbit Coupled Configuration Interaction Approaches. Phys. Chem. Chem. Phys 2013, 15 (19), 7260–7276; [PubMed: 23575467] (b)Roemelt M; Neese F, Excited States of Large Open-Shell Molecules: An Efficient, General, and SpinAdapted Approach Based on a Restricted Open-Shell Ground State Wave function. J. Phys. Chem. A 2013, 117 (14), 3069–3083. [PubMed: 23510206]

40. Neese F, A Spectroscopy Oriented Configuration Interaction Procedure. J. Chem. Phys 2003, 119 (18), 9428–9443.

41. Sure R; Grimme S, Corrected Small Basis Set Hartree-Fock Method for Large Systems. J. Comput. Chem 2013, 34 (19), 1672–1685. [PubMed: 23670872]

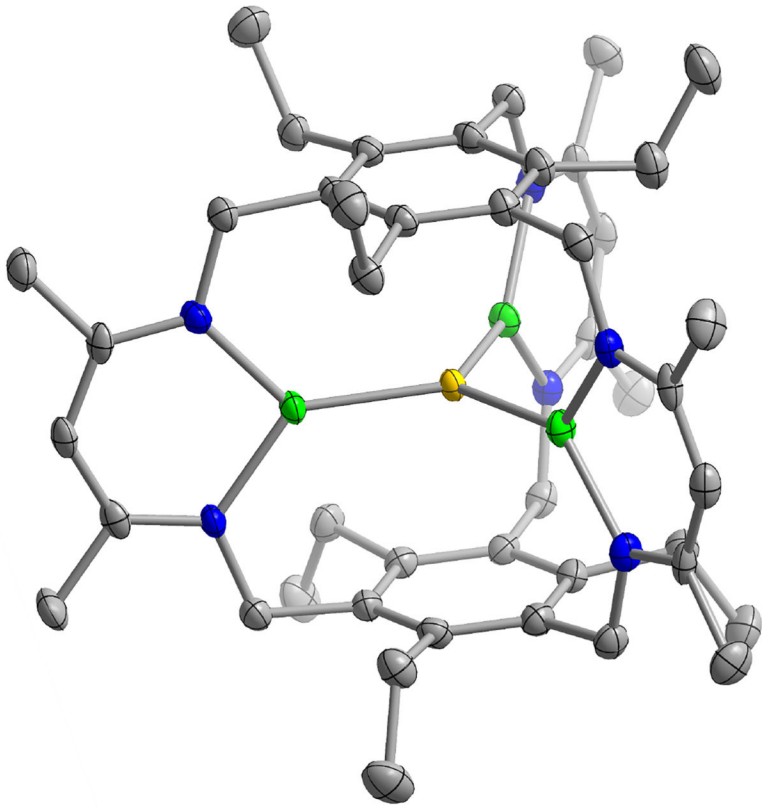

Figure 1.

ORTEP representation of Cu_3Se**L, 4**. Solvent guests and H atoms have been omitted for clarity. Blue, green, yellow-orange, and gray ellipsoids (70% probability) represent N, Cu, Se, and C atoms respectively.

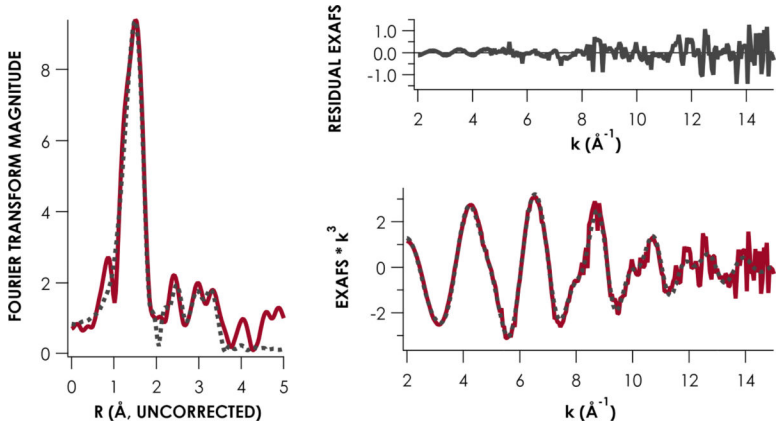

Figure 2.

Fourier transformed k^3-weighted EXAFS (left) and k^3weighted EXAFS (bottom right) of **2**. The experimental data are given as the solid red spectra and the statistically most significant model is given as the dashed black spectra. The top right plot gives the difference between the experimental data and the model for the k^3-weighted EXAFS **2**. Simulation parameters: Shell #1 (Cu-N): n = 2, r = 1.981(3) Å, σ^2 = 0.0045(4) Å^2; Shell #2 (Cu-O): n = 1, r = 1.867(4) Å, σ^2 = 0.0034(6) Å^2; Shell #3 (Cu-C): n = 2, r = 2.72(3) Å, σ^2 = 0.004(1) Å^2; Shell #4 (Cu-C): n = 3, r = 3.449(13) Å, σ^2 = 0.0035(8) Å^2; Shell #5 (Cu-C): n = 3, r = 3.95(3) Å, σ^2 = 0.006(2) Å^2; E_o = 8991.2 eV; ϵ^2 = 0.61.

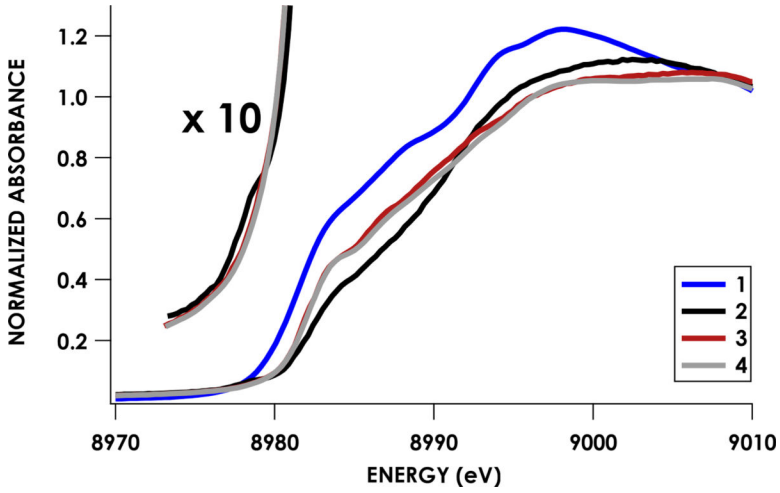

Figure 3.

XANES regions of the Cu K-edge X-ray absorption spectra of 1–4. Pre-edge regions of the spectra obtained for 2–4 are presented as a 10× magnified inset.

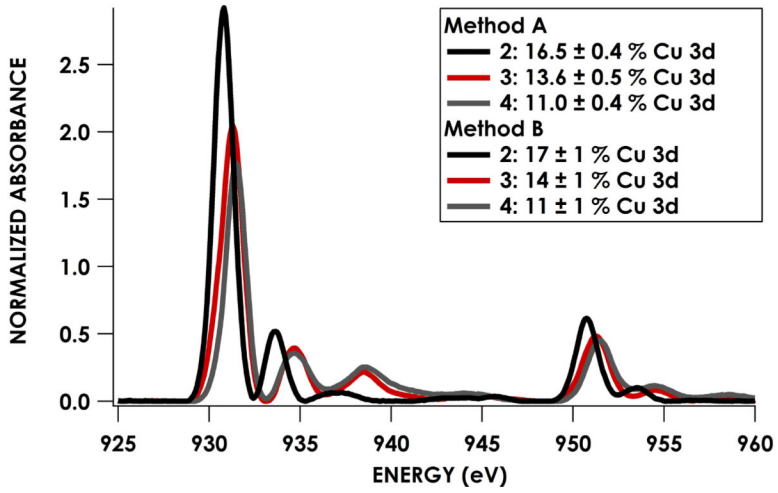

Figure 4.

Cu $L_{2,3}$-edge XAS data obtained for **2**–**4**. % Cu 3*d* contributions to the a_2'' LUMO were determined by comparison of total L_2+L_3 peak areas to that of $(nmph)_2CuCl_4$, for which the Cu 3*d* contribution to the SOMO is 61%.[23b] Errors in Method A obtained from least-squares fitting while those in Method B obtained from applying a 5% error to the total L_3 + L_2 integrated area. Full table of values can be seen in Table S8.

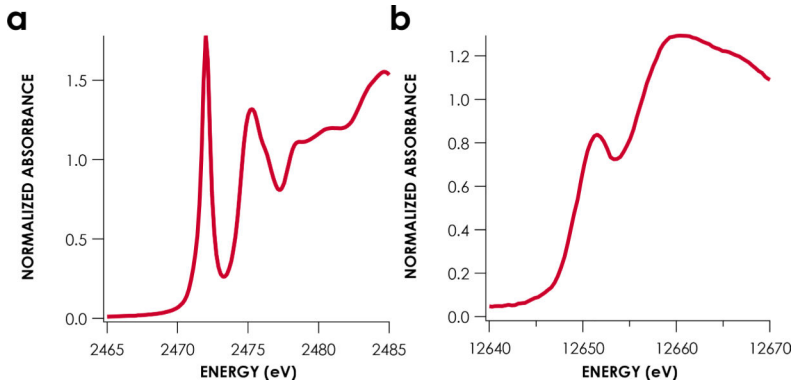

Figure 5.

Ligand K-edge XAS of **2**-**4**. (a) O K-edge XAS of **2** in red with carbon tape substrate shown in black. (b) S K-edge XAS of **3**. (c) Se K-edge XAS of **4**.

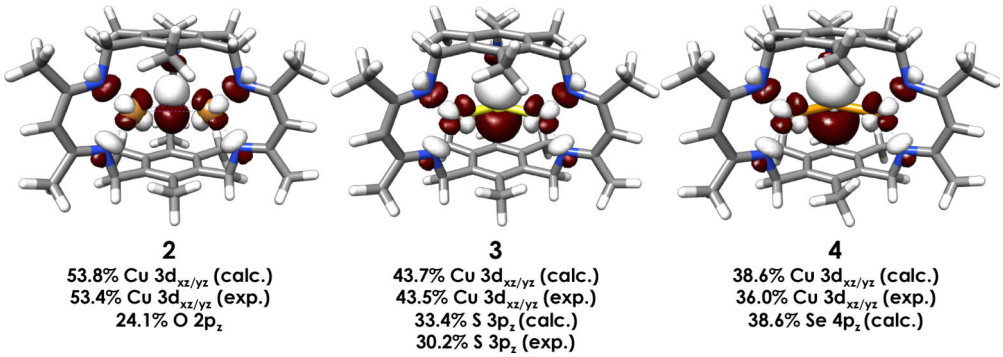

Figure 6.

RKS DFT calculated (PBE0/ZORA-def2-TZVP(-f) with CP(PPP) on Cu) SOMOS for **2'-4'**. Calculated basis orbital contributions to these MOs are printed along with experimentally determined values where available. Orbitals are printed at an isovalue of 0.03.

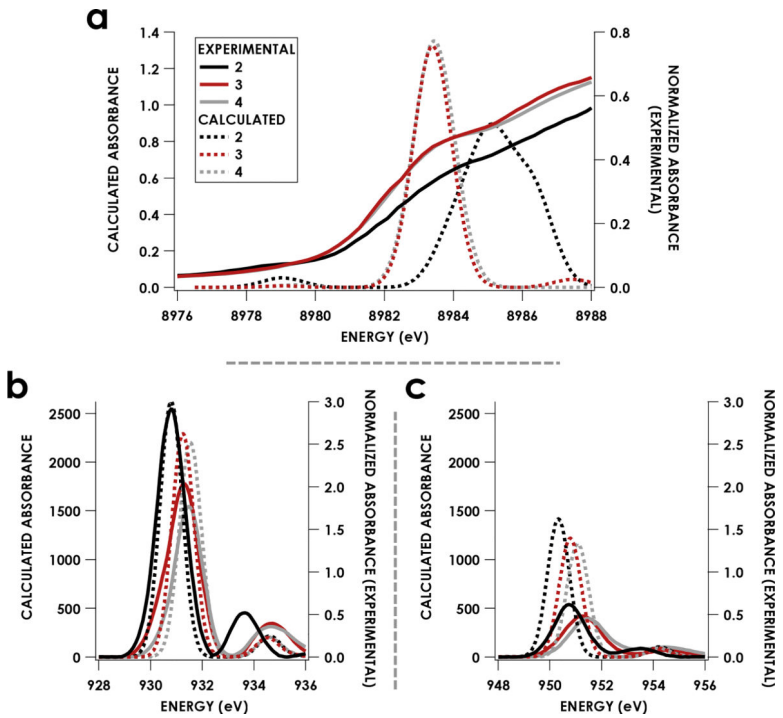

Figure 7.

Experimental (red) and DFT-ROCIS calculated (black dashed) Cu K-edge XAS (a) and O K-edge XAS (b) of **2**. The * in (b) marks the background C-tape carbonyl band. Scalar shifts have been applied to the energies of the calculated spectra to align with experimental values.

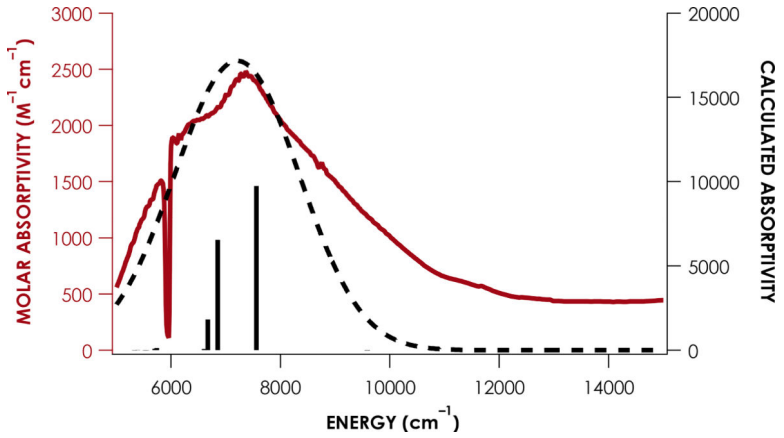

Figure 8.

Experimental (red solid spectrum) and SORCI-calculated (black dashed spectrum) NIR absorption spectrum for **2**. The individual transitions produced by the SORCI calculation are given as gray sticks.

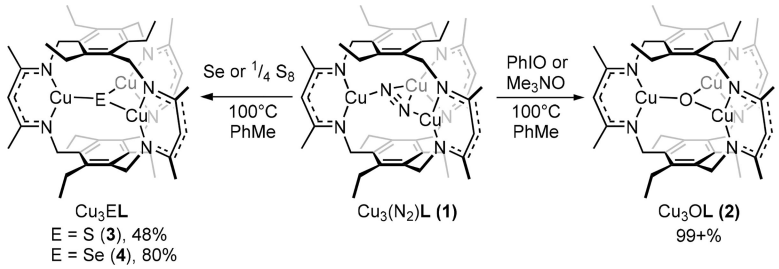

Scheme 1.

Synthesis of CU_3OL (**2**) and selenide congener **(4).**

Table 1.

Bond metrics for 2–4 determined from XAS and XRD.

	2[a] **(Å)**	**3**[b] **(Å)**	**4**[b] **(Å)**
Cu-N	1.981(3)	1.930(3)	1.910(2)
Cu-Cu	n/a	3.649	3.799
Cu-E (E = O, S, Se)	1.867(4)	2.1069(9)	2.1937(4)

[a]Obtained using Cu K-edge EXAFS.

[b]Obtained from X-ray diffraction.

Author Manuscript

Author Manuscript

Author Manuscript

Table 2.

Cu $L_{2,3}$-edge maxima from spectra for 2–4.

Compound	L_3 (eV)	L_2 (eV)	% Cu/hole[a]
2	930.8	950.7	50(1)
3	931.3	951.2	41(1)
4	931.5	951.4	33(1)

[a]Referenced to $(nmph)_2[CuCl_4]$, % Cu 3d/hole = 61%.[23b]